

# ***In-vivo* histology of iron and myelin in the brain**

## **using magnetic susceptibility source separation in MRI**

Hyeong-Geol Shin<sup>1,†</sup>, Jingu Lee<sup>1,2,†</sup>, Young Hyun Yun<sup>3</sup>, Seong Ho Yoo<sup>4</sup>, Jinhee Jang<sup>5</sup>, Se-Hong Oh<sup>6</sup>, Yoonho Nam<sup>6</sup>, Sehoon Jung<sup>7</sup>, Sunhye Kim<sup>7</sup>, Masaki Fukunaga<sup>8</sup>, Woojun Kim<sup>9</sup>, Hyung Jin Choi<sup>10</sup>, and Jongho Lee<sup>1,\*</sup>

<sup>†</sup> These authors equally contributed to this work

### **Author affiliations:**

<sup>1</sup>Laboratory for Imaging Science and Technology, Department of Electrical and Computer Engineering, Seoul National University, Seoul, Republic of Korea

<sup>2</sup>AIRS Medical Inc., Seoul, Republic of Korea

<sup>3</sup>Department of Medicine, Anatomy and Cell Biology, Seoul National University College of Medicine, Seoul, Republic of Korea

<sup>4</sup>Department of Forensic Medicine, Seoul National University College of Medicine, Seoul, Republic of Korea

<sup>5</sup>Department of Radiology, Seoul St Mary's Hospital, College of Medicine, The Catholic University of Korea, Seoul, Republic of Korea

<sup>6</sup>Division of Biomedical Engineering, Hankuk University of Foreign Studies, Yongin, Republic of Korea

<sup>7</sup>Research Institute of Industrial Science and Technology, Pohang, Republic of Korea

<sup>8</sup>Division of Cerebral Integration, National Institute for Physiological Sciences, Okazaki, Japan

<sup>9</sup>Department of Neurology, Seoul St. Mary's Hospital, College of Medicine, The Catholic University of Korea, Seoul, Republic of Korea

<sup>10</sup>Department of Biomedical Sciences, Anatomy and Cell Biology, Neuroscience Research Institute, Wide River Institute of Immunology, Seoul National University College of Medicine, Seoul, Republic of Korea

29

30 **Corresponding Author:**

31 Jongho Lee, Ph.D

32 Department of Electrical and Computer Engineering, Seoul National University

33 Building 301, Room 1008, 1 Gwanak-ro, Gwanak-gu, Seoul, Korea

34 Tel: 82-2-880-7310

35 E-mail: [jonghoyi@snu.ac.kr](mailto:jonghoyi@snu.ac.kr)

36

## 37 ABSTRACT

38 Obtaining a histological fingerprint from the *in-vivo* brain has been a long-standing  
 39 target of magnetic resonance imaging (MRI). In particular, non-invasive imaging of iron and  
 40 myelin, which are involved in normal brain functions and are histopathological hallmarks in a  
 41 few neurodegenerative diseases, has practical utilities in neuroscience and medicine. Here,  
 42 we propose a biophysical model that describes the individual contribution of iron and myelin  
 43 to MRI signals via their difference in magnetic susceptibility (i.e., paramagnetic iron vs.  
 44 diamagnetic myelin). Using this model, we develop a method,  $\chi$ -separation, that generates  
 45 the voxel-wise distributions of iron and myelin. The method is validated using computer  
 46 simulation and phantom experiments, and applied to *ex-vivo* and *in-vivo* brains. The results  
 47 delineate the well-known histological features of iron and myelin in the specimen (e.g., co-  
 48 localization of iron and myelin in Gennari line), healthy volunteers (e.g., myelin-lacking and  
 49 iron-rich pulvinar), and multiple sclerosis patients (e.g., demyelinated iron-rim lesion). This  
 50 new *in-vivo* histology technology, taking less than 20 min, may serve as a practical tool for  
 51 exploring the microstructural information of the brain.

52

## 53 Keywords:

54 Magnetic Resonance Imaging (MRI), In-vivo histology, Quantitative susceptibility  
 55 mapping,  $\chi$ -separation, Magnetic susceptibility source separation, Iron imaging, Myelin  
 56 imaging, quantitative MRI.

57

## 58 Introduction

59 In neuroscience, histology has provided rich information of microscopic brain  
60 anatomy, assisting to discover neuron<sup>1</sup> and parcellate cerebral cortex<sup>2</sup>. Even today, we rely on  
61 histology in exploring microscale pathogenesis of neurological diseases<sup>3</sup> or identifying  
62 cortical myeloarchitecture and subcortical nuclei<sup>4</sup>. Despite the utility of histology, it  
63 inevitably entails a tissue invasion, limiting the opportunity of applying the technology to the  
64 *in-vivo* brain.

65 Magnetic resonance imaging (MRI) is a powerful non-invasive tool for visualizing  
66 brain anatomy and function. Various image contrasts of MRI provide the physical  
67 information of tissues such as T<sub>1</sub> relaxation, T<sub>2</sub> relaxation, and diffusion. Recently, efforts  
68 have been made to build connections between MRI measurements and microstructural  
69 properties of the brain (e.g., neurite density and myelination) that are not directly available at  
70 an MRI resolution<sup>5-7</sup>. These approaches allow us to estimate voxel-averaged microstructural  
71 information of the *in-vivo* brain that used to be accessible only via *ex-vivo* histology.

72 One of the promising contrasts for the new technology, which is referred to as *in-vivo*  
73 histology, is magnetic susceptibility, measured by T<sub>2</sub>\* decay and/or phase evolution<sup>8,9</sup>. The  
74 contrast was utilized to reveal laminar structures in cortices (e.g., stria of Gennari<sup>9</sup>), tiny  
75 nuclei in subcortices (e.g., nigrosome 1 and 4<sup>10</sup>), and variations of iron concentration in  
76 superficial white matter<sup>11</sup>.

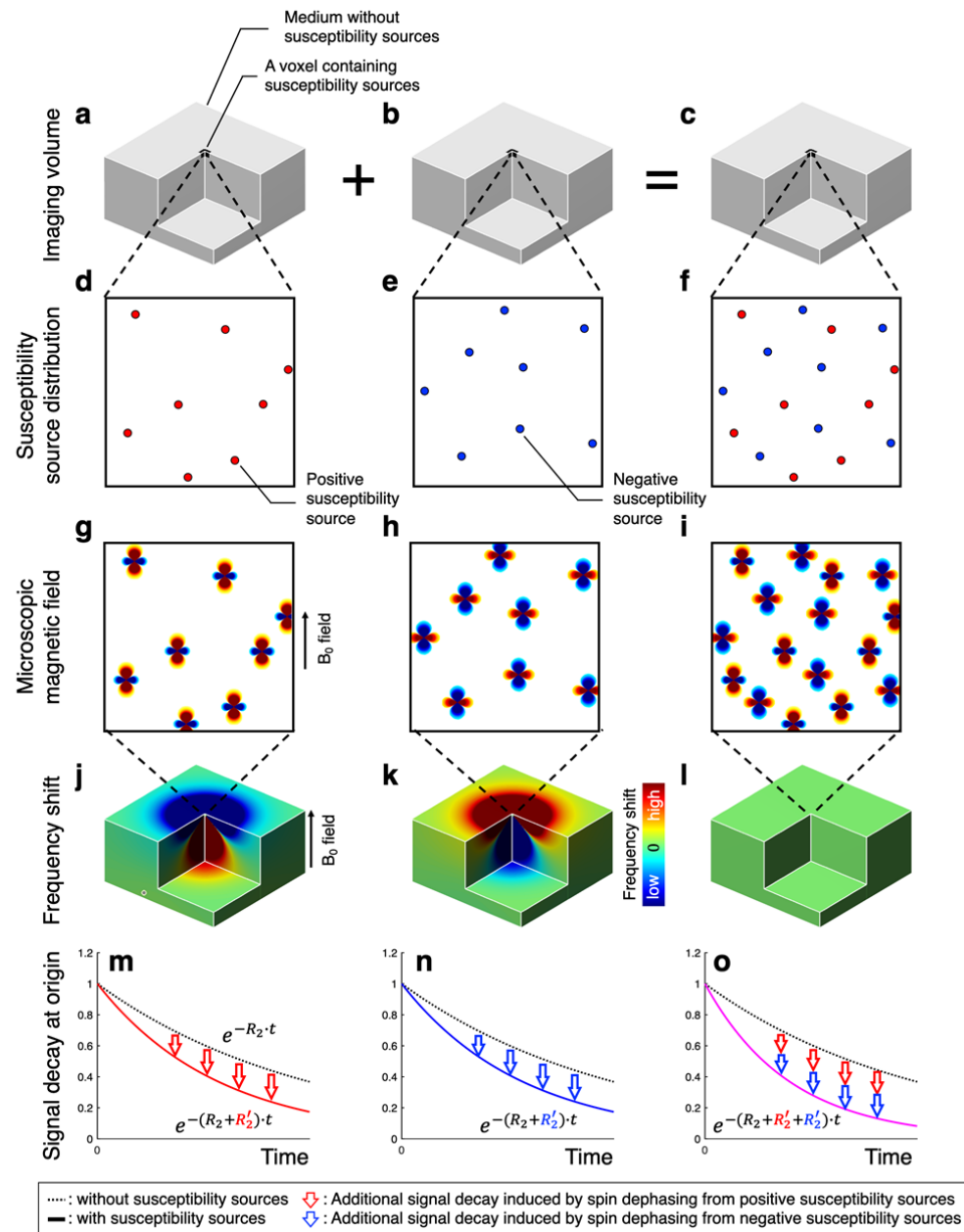
77 In the brain, the susceptibility contrast has been demonstrated to originate primarily  
78 from two sources: iron and myelin<sup>12</sup>. These substances have essential roles in normal brain  
79 functions. For example, iron is known to contribute to the synthesis of myelin, DNA, and  
80 neurotransmitters<sup>13</sup>. Changes in iron homeostasis are related to the pathogenesis of multiple  
81 sclerosis (MS), Alzheimer's diseases (AD), and Parkinson's disease<sup>14,15</sup>. For myelin,  
82 production and degradation have shown to be involved in development<sup>16</sup>, neuro-plasticity<sup>17</sup>,  
83 and neurodegenerative diseases such as MS and leukodystrophy<sup>18,19</sup>. As a result, the two  
84 substances have been suggested as important biomarkers for neurological disorders.

85 Interestingly, iron and myelin have the opposite magnetic susceptibility  
86 characteristics: paramagnetic iron vs. diamagnetic myelin. This difference may provide an  
87 opportunity to differentiate the substances. However, measuring the individual concentration

is still challenging because they co-exist in most of the brain regions and collectively determine the susceptibility contrasts<sup>20,21</sup>. Efforts have been made to separate the contributions of iron and myelin. Schweser et al. suggested to quantify regional iron in quantitative susceptibility mapping (QSM) by removing myelin contribution measured by magnetization transfer<sup>22</sup>. Stüber et al. proposed to infer iron and myelin concentrations via a multivariate linear regression analysis between  $R_1$  and  $R_2^*$  vs. iron and myelin concentrations measured by proton-induced X-ray emission<sup>23</sup>. In these studies, however, the relation between the MRI measurements and the two substances were determined empirically rather than via biophysical modeling.

In this work, we formulate a new biophysical model that explains the individual contribution of paramagnetic (e.g., iron) and diamagnetic (e.g., myelin) susceptibility sources to MRI signals. By exploiting the model, we develop a new susceptibility source separation method,  $\chi$ -separation, which estimates the individual concentration of the two sources even when they co-exist in a voxel. Our biophysical model and  $\chi$ -separation method are validated using a numerical simulation and an experimental phantom. Then, the  $\chi$ -separation method is tested for its specificity to iron and myelin using an *ex-vivo* human brain specimen by comparing the  $\chi$ -separation results with an iron image from laser ablation-inductively coupled plasma-mass spectrometry (LA-ICP-MS) and a myelin image from Luxol fast blue (LFB) stain. Finally, the method is applied to the *in-vivo* human brain, revealing histologically well-known features of iron and myelin. In MS patients, the  $\chi$ -separation results suggest to characterize lesion types, demonstrating the feasibility of applying the method for clinical research.

# 111 RESULTS



112

113 **Figure 1. Conceptual illustration of MRI resonance frequency shift and transverse**  
 114 **signal decay from positive and negative susceptibility sources. a-c,** Imaging volume with a  
 115 voxel at the origin containing randomly distributed spherical susceptibility sources. The  
 116 sources have positive susceptibility in the first column, negative susceptibility in the second  
 117 column, and both positive and negative susceptibility in the third column. **d-f,** Microscopic  
 118 view of the susceptibility source distribution. **g-i,** Magnetic field perturbation induced by the

susceptibility sources when the  $B_0$  field is applied. **j-l**, Voxel-averaged frequency shift in the imaging volume. The frequency shift is zero when the same amounts of the positive and negative susceptibility sources exist in the voxel (**l**). **m-o**, Transverse signal decay with irreversible ( $R_2$ ) and reversible ( $R_2'$ ) transverse relaxation rates in the voxel at the origin. The voxel containing both positive and negative susceptibility sources show  $R_2'$  as the sum of  $R_2'$  from the positive-source-only voxel and the negative-source-only voxel (**o**).

### **Biophysical model for $\chi$ -separation**

When a susceptibility source is positioned in a magnetic field, the field within and around the source is perturbed according to Maxwell's equations (Fig. 1). This field perturbation creates variations in the resonance frequency of MRI. The frequency shift ( $\Delta f$ ), originating from a bulk magnetic susceptibility distribution ( $\chi(\mathbf{r})$ ), has been modeled as follows<sup>24</sup>:

$$\Delta f(\mathbf{r}) = D_f(\mathbf{r}) * \chi(\mathbf{r}) \quad [\text{Eq. 1}]$$

where  $\mathbf{r}$  is the position vector of a voxel,  $D_f$  is a field perturbation kernel, and  $*$  denotes a convolution operation. The kernel can be analytically derived from Maxwell's magneto-static equations<sup>24,25</sup> and has a well-known field pattern of a magnetic dipole. In conventional QSM,  $\Delta f$  is obtained from the phase of an MRI signal, and then  $\chi$  is estimated by the deconvolution of  $D_f$  from  $\Delta f$ <sup>26,27</sup>.

If a voxel contains both paramagnetic and diamagnetic susceptibility sources, the bulk magnetic susceptibility can be expressed as the sum of positive susceptibility (i.e.,  $\chi_{pos} > 0$ ) and negative susceptibility (i.e.,  $\chi_{neg} < 0$ ) of the voxel. Then, the frequency shift can be expressed as the signed sum of the effects of two susceptibility sources. Therefore, Eq. 1 can be written as follows:

$$\Delta f(\mathbf{r}) = D_f(\mathbf{r}) * (\chi_{pos}(\mathbf{r}) + \chi_{neg}(\mathbf{r})). \quad [\text{Eq. 2}]$$

The decay of a transverse MRI signal has been described by two different time constants,  $R_2$  and  $R_2'$ , which are referred to as irreversible and reversible transverse relaxation rates, respectively. The  $R_2'$  relaxation originates primarily from magnetic

susceptibility sources when ignoring chemical exchange and chemical shift effects. In the static dephasing regime, which postulates low diffusivity and low susceptibility source concentration, the decay of a voxel can be modeled as follows<sup>21</sup> :

$$R_2'(\mathbf{r}) = D_r(\mathbf{r}) \cdot |\chi(\mathbf{r})| \quad [\text{Eq. 3}]$$

where  $D_r$  is a relaxometric constant between  $R_2'$  and susceptibility. This equation suggests that  $R_2'$  is linearly proportional to the concentration of susceptibility sources regardless of the sign of them. The relaxometric constant can be estimated by the ratio of  $R_2'$  to absolute susceptibility.

The  $R_2'$  model in Eq. 3 can be extended to consider a voxel that contains both positive and negative susceptibility sources (see Supplementary Note):

$$R_2'(\mathbf{r}) = D_{r,pos}(\mathbf{r}) \cdot |\chi_{pos}(\mathbf{r})| + D_{r,neg}(\mathbf{r}) \cdot |\chi_{neg}(\mathbf{r})| \quad [\text{Eq. 4}]$$

where  $D_{r,pos}$  and  $D_{r,neg}$  are the relaxometric constants for the positive and negative susceptibility sources, respectively. An important implication of this equation is that  $R_2'$  is determined by the (weighted) absolute sum of the effects of the two susceptibility sources.

Using Eqs. 2 and 4, the effects of magnetic susceptibility on a complex MRI signal can be modeled as follows:

$$R_2'(\mathbf{r}) + i2\pi \cdot \Delta f(\mathbf{r}) = \overline{D_{r,pos}} \cdot |\chi_{pos}(\mathbf{r})| + \overline{D_{r,neg}} \cdot |\chi_{neg}(\mathbf{r})| + i2\pi D_f(\mathbf{r}) * (\chi_{pos}(\mathbf{r}) + \chi_{neg}(\mathbf{r})) \quad [\text{Eq. 5}]$$

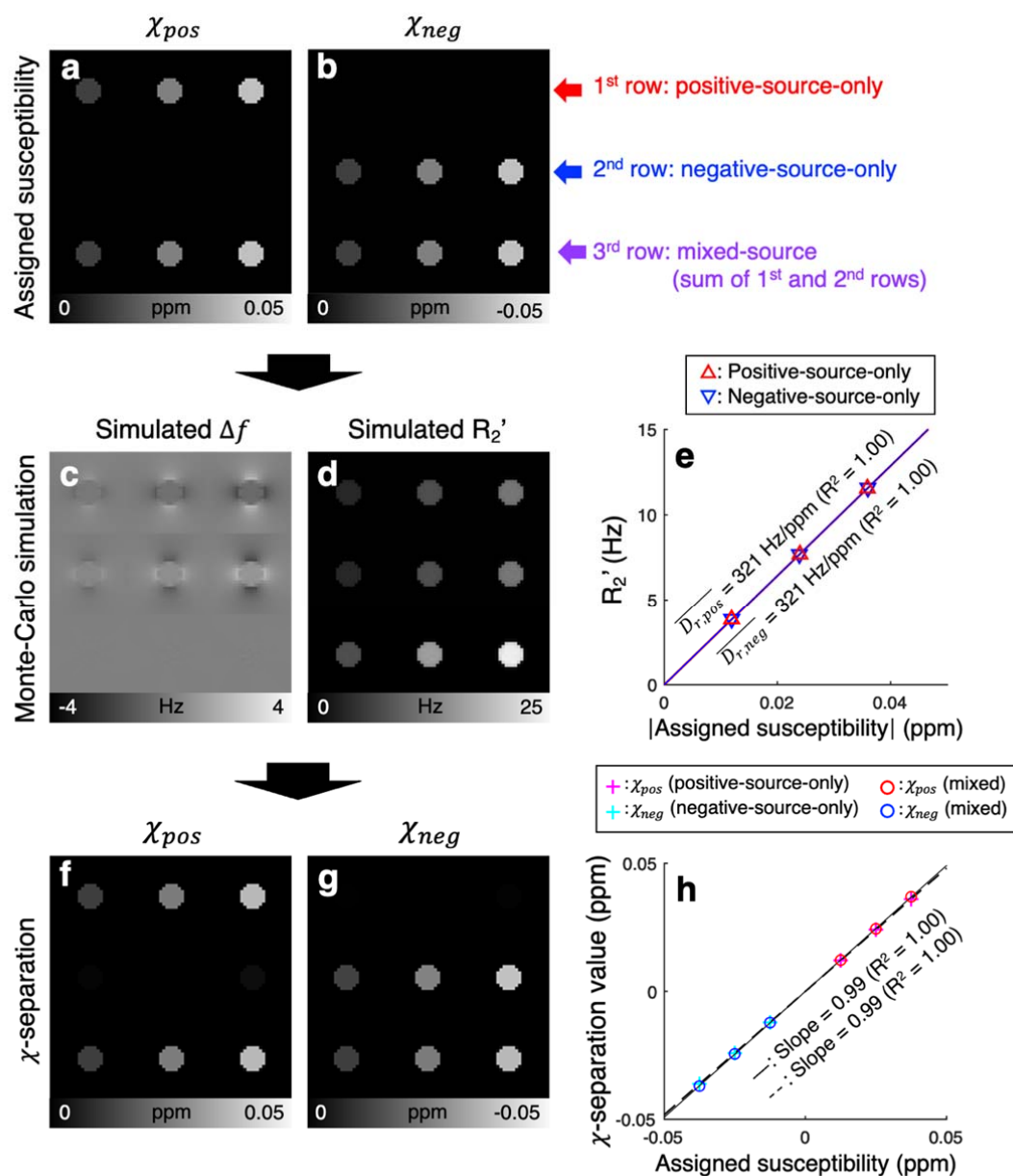
where  $\overline{D_{r,pos}}$  and  $\overline{D_{r,neg}}$  are nominal relaxometric constants for the positive and negative susceptibility sources, respectively, assuming spatial invariance. By solving Eq. 5, we can obtain the distributions of the positive and negative magnetic susceptibility sources. For details of implementation, see Supplementary Information.

### **Monte-Carlo simulation for validation**

To demonstrate the validity of our susceptibility model (Eqs. 2 and 4) and  $\chi$ -separation method, Monte-Carlo simulation is performed and the results are summarized in



Fig. 2 and Supplementary Figure 2. Nine cylinders with different combinations of susceptibility source compositions (first row: positive-source-only, second row: negative-source-only, and third row: sum of the positive and negative sources) and susceptibility concentrations are designed as shown in Fig. 2a-b. The resulting frequency shift maps demonstrate that the magnetic field perturbations around the positive-source-only cylinders and the negative-source-only cylinders show the dipole patterns as suggested in Eq. 1 (Fig. 2c). The  $R_2'$  maps, on the other hand, reveal localized  $R_2'$  within the source-containing voxels (Fig. 2d). The cylinders in the last row, containing the mixtures of the positive and negative susceptibility sources, demonstrate zero frequency shift in the frequency shift maps, while the  $R_2'$  maps report the contrasts proportional to the absolute sum of the positive and negative susceptibility (Supplementary Figure 2). These observations validate our susceptibility model, which states that the signed sum of  $\chi_{pos}$  and  $\chi_{neg}$  determines the frequency shift while the absolute sum of them decides  $R_2'$ . The positive and negative relaxometric constants are measured as 321 Hz/ppm (Fig. 2e). When  $\chi$ -separation is applied to the Monte-Carlo simulated frequency shift and  $R_2'$  maps, the positive and negative susceptibility maps demonstrate successful separation of the two sources as demonstrated in Fig. 2f-g. The linear regression result confirms the accuracy of the  $\chi$ -separation results (assigned susceptibility vs. measured susceptibility in the single-source-only cylinders: slope = 0.99,  $R^2 = 1.00$ , dashed line in Fig. 2h; assigned susceptibility vs. measured susceptibility in the mixed-source cylinders: slope = 0.99,  $R^2 = 1.00$ , solid line in Fig. 2h; slight underestimation from the numerical errors in the dipole kernel calculation).



194

195 **Figure 2. Validation of  $\chi$ -separation using the Monte-Carlo simulation.** **a-b**, Positive and  
 196 negative susceptibility maps assigned for the simulation. **c-d**, Frequency shift ( $\Delta f$ ) and  $R_2'$   
 197 maps generated from the simulation. **e**, Absolute values of the assigned susceptibility vs.  $R_2'$   
 198 (red upper triangles: positive-source-only cylinders; blue lower triangles: negative-source-  
 199 only cylinders). Both of the relaxometric constants are 321 Hz/ppm ( $R^2 = 1.00$ ). **f-g**, Positive  
 200 and negative susceptibility maps reconstructed from  $\chi$ -separation. The  $\chi$ -separation results  
 201 demonstrate a successful reconstruction of the assigned susceptibility. **h**, Assigned

susceptibility vs.  $\chi$ -separation results (magenta crosses: positive susceptibility in the positive-source-only cylinders; cyan crosses: negative susceptibility in the negative-source-only cylinders; red circles: positive susceptibility in the mixed-source cylinders; blue circles: negative susceptibility in the mixed-source cylinders). The susceptibility values from  $\chi$ -separation match well with the assigned susceptibility values (regression results of assigned vs. single-source-only cylinder measurements: slope = 0.99 with  $R^2 = 1.00$ , dashed line; regression results of assigned vs. mixed-source cylinder measurements: slope = 0.99 with  $R^2 = 1.00$ , solid line)

### ***Phantom experiment for validation***

A phantom experiment using the positive ( $\text{Fe}_3\text{O}_4$ ) and negative ( $\text{CaCO}_3$ ) susceptibility sources further consolidates the validity of our model and  $\chi$ -separation. Figure 3c shows the arrangement of the phantom with the different compositions of  $\text{Fe}_3\text{O}_4$  and  $\text{CaCO}_3$  (first row: positive-source-only, second row: negative-source-only, and third row: sum of the positive and negative sources). The frequency shift map demonstrates the opposite field patterns between the positive (first-row) and negative (second-row) susceptibility sources (Fig. 3a). The third row, containing both sources, shows no conspicuous frequency shift, suggesting the signed sum of the susceptibility sources determines the frequency shift. On the other hand,  $R_2'$  reports dependence not on the signed sum but on the absolute sum of the susceptibility sources (Fig. 3b and Supplementary Figure 3). The relaxometric constants are measured as 275 Hz/ppm ( $\overline{D_{r,pos}}$ ;  $R^2 = 1.00$ ) for the positive source and 291 Hz/ppm ( $\overline{D_{r,neg}}$ ;  $R^2 = 0.83$ ) for the negative source (Supplementary Figure 4). When  $\chi$ -separation is applied, the results demonstrate successful separation of the two sources, revealing the positive susceptibility in the first and third cylinders and the negative susceptibility in the second and third cylinders (Fig. 3d-e). The linear regression results in Figure 3f show that the susceptibility values in the positive-source-only and negative-source-only cylinders agree with those in the mixed-source cylinders, confirming the validity of  $\chi$ -separation (slope = 0.94;  $R^2 = 1.00$ ).

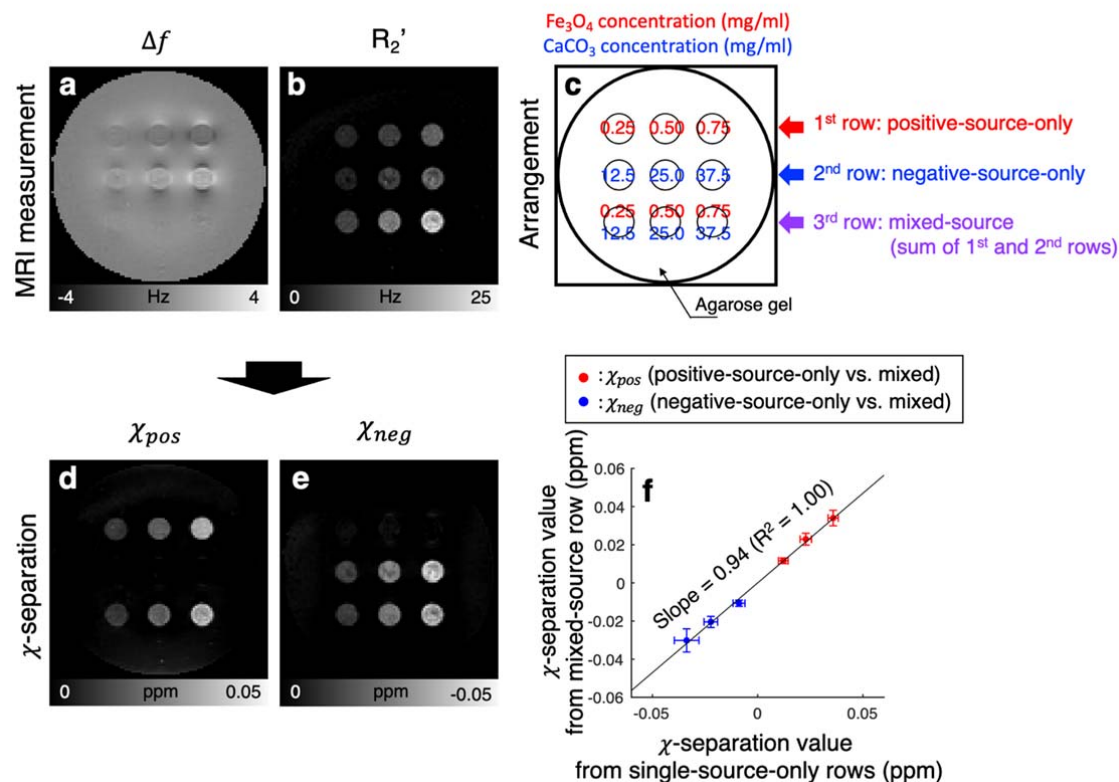


**Figure 3. Validation of  $\chi$ -separation using the phantom experiment.** a-b, Frequency shift and  $R_2'$  maps from MRI measurements. c, Assigned susceptibility source concentrations (Fe<sub>3</sub>O<sub>4</sub> for the positive susceptibility source and CaCO<sub>3</sub> for the negative susceptibility source) d-e, Positive and negative susceptibility maps reconstructed from  $\chi$ -separation. The results demonstrate successful separation of the two sources. f, Susceptibility measurements in the single-source-only cylinders vs. mixed-source cylinders (red dots: positive susceptibility in positive-source-only cylinders vs. mixed-source cylinders; blue dots: negative susceptibility in negative-source-only cylinders vs. mixed-source cylinders). The susceptibility values from the mixed-source cylinders match well with those from the single-source-only cylinders (regression results: slope = 0.94 with  $R^2$  of 1.00). Vertical and horizontal error bars in (f) indicate the standard deviation of the measurements in each cylinder.

### Ex-vivo brain specimen

When  $\chi$ -separation is applied to an *ex-vivo* brain specimen containing the primary

visual cortex (V1), the positive and negative susceptibility maps reveal great similarities to the iron image from LA-ICP-MS and the myelin image from LFB myelin staining, respectively (Fig. 4; see Supplementary Figure 5 for zoomed-in) despite complex microscopic environment of the brain (see Discussion). Overall, the cortex shows higher positive susceptibility and lower negative susceptibility than white matter (Fig. 4c-d). These patterns are in good agreement with the iron and myelin images in Fig. 4e and f. In V1, which is near the calcarine fissure outlined by the green lines, distinct laminar patterns are captured in the positive and negative susceptibility maps. The positive susceptibility map (Fig. 4c) shows three distinct layers, which reveal very low intensity in the superficial layer, an intensity peak in the middle layer (yellow arrows), and high intensity in the deep layer. These patterns are well-recognized in the iron image (Fig. 4e). In both images, the intensity peak disappears in the secondary visual cortex (V2). Compared to the positive susceptibility map, the negative susceptibility map (Fig. 4d) demonstrates a different pattern that illustrates low intensity in the superficial layer, an intensity peak in the middle layer, and low intensity in the deep layer, agreeing with the myelin histology image (Fig. 4f). The distinct peak in the middle layer of both susceptibility maps (Fig. 4c-d, yellow arrowheads) coincides with the previously reported histological characteristics of the stria of Gennari, featuring the co-existence of high concentration of iron and myelin (see Supplementary Figure 5 for a zoomed-in image)<sup>28</sup>. Intensity variations in the susceptibility maps are also observed in white matter and are in accordance with the iron and myelin images. In particular, stratum sagittale internum (purple squares in Fig. 4c-d) reports higher positive susceptibility and lower negative susceptibility than the surrounding white matter regions (red triangles: optic radiation; green stars: forceps), agreeing with the iron and myelin images (Fig. 4e-f) and previous reports<sup>12,29</sup>. On the other hand, these histological features are scantily observable or interpretable in the conventional contrasts (Fig. 4a-b).

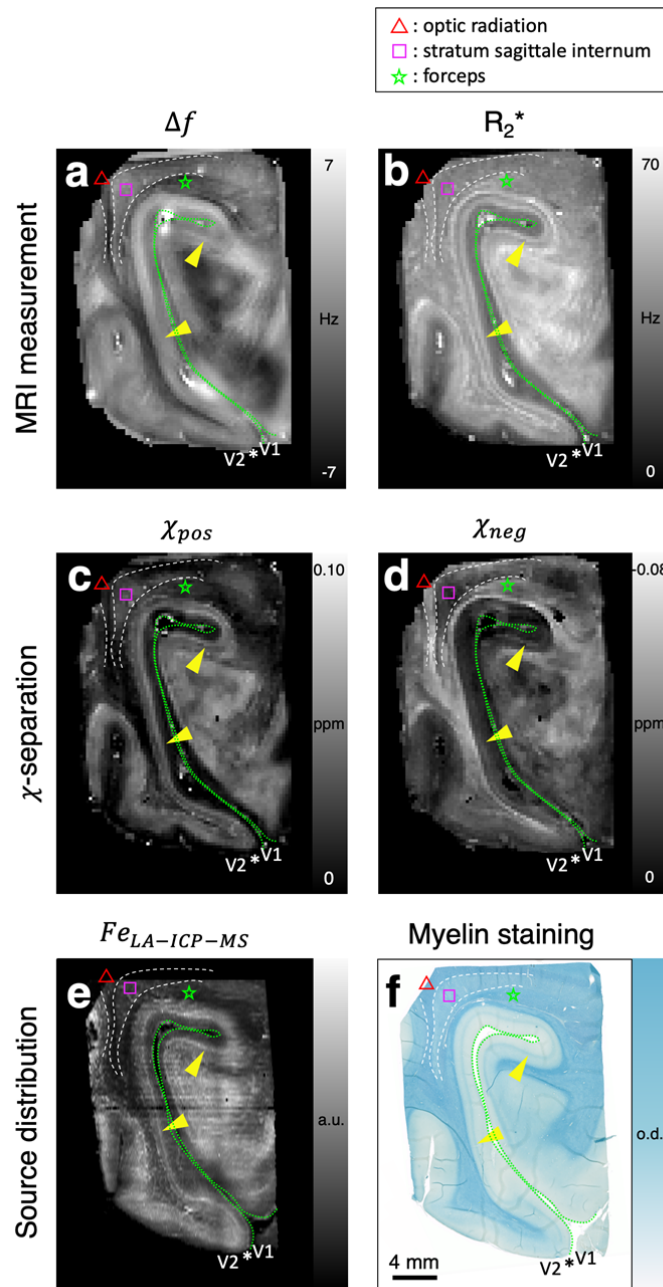


**Figure 4. Comparison between  $\chi$ -separation maps vs. iron and myelin images in the human brain specimen containing V1.** a-b, Frequency shift and  $R_2^*$  maps from MRI measurements. c-d, Positive ( $\chi_{pos}$ ) and negative susceptibility ( $\chi_{neg}$ ) maps from  $\chi$ -separation. e, Iron image from LA-ICP-MS ( $Fe_{LA-ICP-MS}$ ). f, Myelin image from LFB myelin staining. The positive susceptibility map reveals similar contrasts to the iron image whereas the

negative susceptibility map shows similar features to the myelin image. Yellow arrowheads point the stria of Gennari that shows high concentrations of iron and myelin (see Supplementary Figure 5 for zoomed-in). Asterisks indicate V1-V2 boundaries. The pial surfaces of the calcarine fissure are delineated by green dashed lines. Red triangles, purple squares, and green stars mark optic radiation, stratum sagittale internum, and forceps, respectively. These white matter fibers show different concentrations of iron and myelin (e-f) which correspond well with the  $\chi$ -separation results (c-d).

### ***Healthy volunteers***

When  $\chi$ -separation is applied to healthy volunteers, the positive and negative susceptibility maps (Figure 5 for a whole-brain slice and Figure 6 for a few zoomed-in regions) render well-known characteristics of iron and myelin distributions that are not available in conventional contrasts (Fig. 5a-c and Supplementary Figure 6), suggesting the utility of  $\chi$ -separation *in vivo*. For example, the deep gray matter regions show not only high positive susceptibility but also low negative susceptibility concentrations (yellow arrows in Fig. 5d-e), agreeing with high iron and low myelin concentrations in the areas<sup>30,31</sup>. In the negative susceptibility map, white matter reveals high signal intensity. In particular, optic radiation and forceps major (green and blue arrows in Fig. 5e), which are known to have high concentrations of myelin<sup>29</sup>, demonstrate high negative susceptibility concentrations. On the other hand, cortical gray matter shows low signal intensity in the negative susceptibility map, agreeing with our myelin histology (Fig. 4f). The total susceptibility map (Fig. 5f) demonstrates good similarities to the conventional QSM map (Fig. 5c). When analyzed for a few regions of interest (ROIs), the results from the positive susceptibility map better explains the literature values of iron concentrations than those of the conventional QSM (Supplementary Figure 7). The relaxometric constant is estimated as 137 Hz/ppm with  $R^2$  of 0.70 (Supplementary Figure 8).



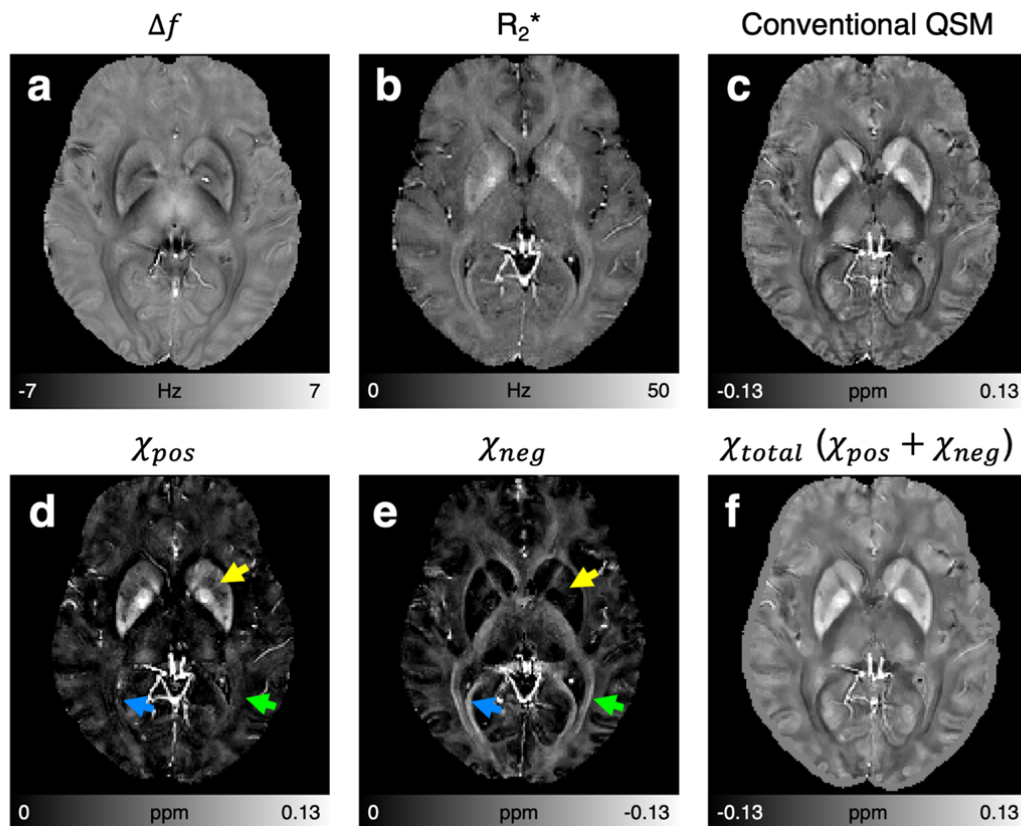


**Figure 5. *In-vivo* results of a healthy volunteer.** **a-c**, Frequency shift,  $R_2^*$ , and conventional QSM maps. **d-e**, Positive and negative susceptibility maps from  $\chi$ -separation, reporting well-known iron and myelin distributions (e.g. high iron but low myelin concentrations in deep gray matter; high myelin concentrations in optic radiation and forceps major) that are not available in the conventional contrasts. Yellow, green, and blue arrows indicate deep gray matter, optic radiation, and forceps major, respectively. **f**, Total susceptibility map calculated as the sum of the positive and negative susceptibility maps.

When the *in-vivo*  $\chi$ -separation maps of the basal ganglia, thalamus, and midbrain areas are zoomed-in and compared with the histology images from the literatures<sup>30-32</sup>, the positive and negative susceptibility maps match well with the iron and myelin histology results, respectively (Fig. 6). In basal ganglia (Fig. 6a-d), hyperintense positive susceptibility and hypointense negative susceptibility are observed in iron-rich but myelin-deficient regions including caudate nucleus (CN), globus pallidus (GP), and putamen (Put). On the other hand,



hyperintensity in the negative susceptibility map (Fig. 6c) is observed in myelin-rich regions, depicting anterior limb of internal capsule (ALIC), external capsule (EC), fornix (Fx), and posterior limb of internal capsule (PLIC). In thalamus (Fig. 6e-h), the two sub-thalamic nuclei, pulvinar (Pul) and nucleus dorsomedialis (ND) where myelin concentrations are low (arrows in Fig. 6h), are identified in the negative susceptibility map (arrows in Fig. 6g). In particular, Pul shows high iron concentration (Fig. 6e), which is also observed in the positive susceptibility map (Fig. 6f). The rest of the thalamus reveals both positive and negative susceptibility sources that are supported by the iron and myelin histology images. In midbrain (Fig. 6i-l), red nucleus (RN) and substantia nigra (SN) show high iron but low myelin concentrations in histology. These variations are well-demonstrated in the positive and negative susceptibility maps (Fig. 6j-k) while the opposite characteristics being observed in crus cerebri (CrC).

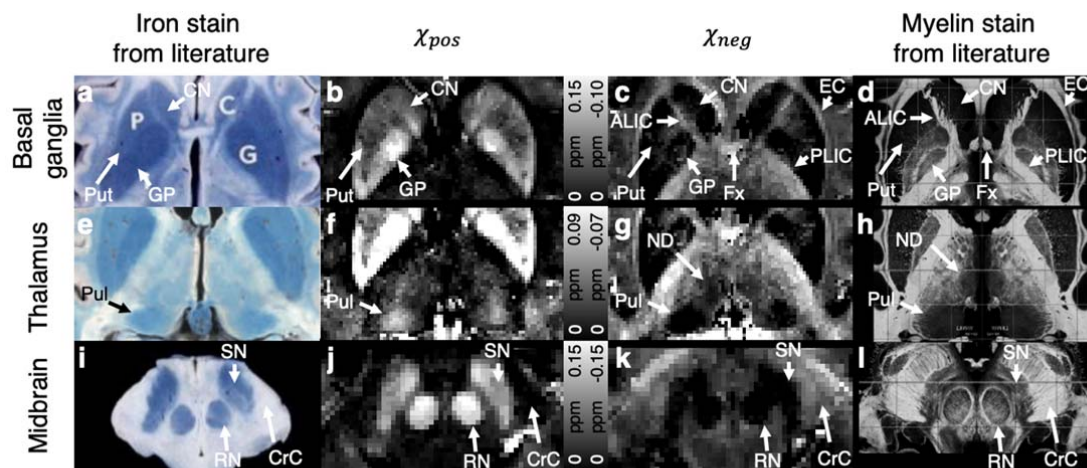


**Figure 6. Comparison between *in-vivo*  $\chi$ -separation results vs. iron and myelin histology from literatures.** Zoom-in images of (a-d) basal ganglia, (e-h) thalamus, and (i-l) midbrain with (a, e, i) iron staining images, (b, f, j) positive susceptibility maps of  $\chi$ -separation, (c, g, k) negative susceptibility maps of  $\chi$ -separation, and (d, h, l) myelin staining images. Similar distributions are observed between the positive susceptibility maps and the iron staining images as well as the negative susceptibility maps and the myelin staining images. The  $\chi$ -separation results reveal exquisite details of the brain anatomy that match with the iron and

myelin histology: ALIC - anterior limb of internal capsule, CN - caudate nucleus, CrC - crus cerebri, EC - external capsule, Fx - fornix, GP - globus pallidus, ND - nucleus dorsomedialis, PLIC - Posterior limb of internal capsule, Pul - pulvinar, Put - putamen, RN - red nucleus, and SN - substantia nigra. Histological images are reproduced from Drayer et al.<sup>30</sup> (a, i), Naidich et al.<sup>32</sup> (e), and Schaltenbrand-Wahren<sup>31</sup> (d, h, l). For visualization, the myelin staining images were intensity-inverted and replicated with the left-right symmetry.

### ***Multiple sclerosis patients***

The results from two MS patients in Fig. 7 demonstrate the application of  $\chi$ -separation in characterizing MS lesions. A lesion in Patient 1 (Fig. 7a, white box) renders rim-shaped hyperintensity in the positive susceptibility map (Fig. 7b) and overall hypointensity in the negative susceptibility map (Fig. 7c). These observations agree with the characteristics of the well-known “iron-rim lesion,” which has iron accumulation at the lesion boundary and demyelination in the lesion core<sup>33</sup>. Different from this lesion, a lesion in Patient 2 (Fig. 7g, white box) show hypointensity in both positive and negative susceptibility maps (Fig. 7h-i). These patterns are in line with the histology of another popular lesion subtype, which has demyelination and iron depletion in the lesion<sup>34</sup>. In the conventional contrasts (Fig. 7d-f and j-l), however, these interpretations are not possible because the contrasts measure the combined effects of iron and myelin.

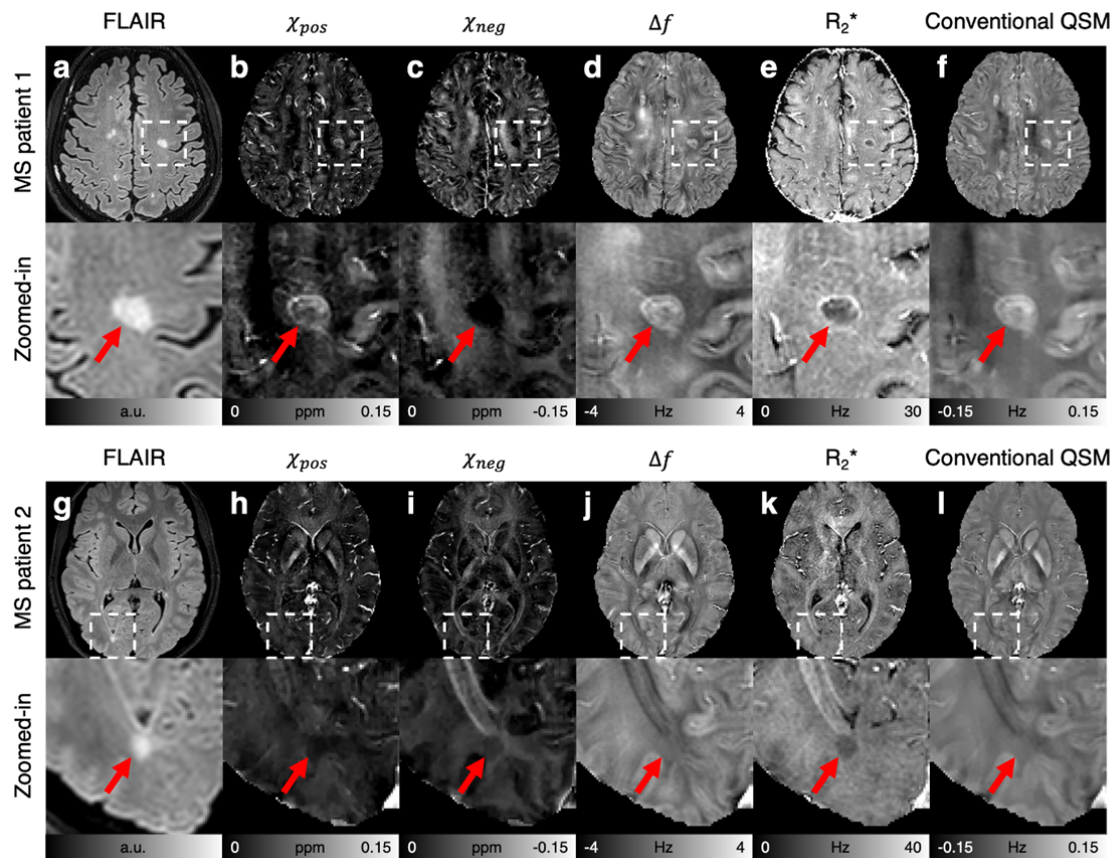


**Figure 7. In-vivo results of two MS patients with characteristic lesions. a and g, FLAIR images. b and h, Positive susceptibility maps. c and i, Negative susceptibility maps. d and j, Frequency shift maps. e and k,  $R_2^*$  maps. f and l, Conventional QSM maps. The zoom-in images show the areas (white boxes) containing typical MS lesions (MS patient 1: demyelinated iron-rim lesion; MS patient 2: demyelinated lesion with iron depletion). Red arrows indicate the location of the lesions in the FLAIR images.**

## DISCUSSION

The newly proposed method,  $\chi$ -separation, reveals the details of brain anatomy that are not easily visible in conventional MR images. In particular, the clear delineation of subthalamic nuclei and midbrain structures (Fig. 6) may provide valuable information in such applications as deep brain stimulation<sup>35</sup> and focused ultrasound surgery<sup>36</sup>. Similarly,  $\chi$ -separation images can be used as inputs for multi-contrast brain parcellation<sup>37</sup>, providing a subject-specific localization of subthalamic nuclei and midbrain structures. The localization may be used to detect the volume change of subthalamic nuclei in psychosis<sup>38</sup>. In MS research, the iron and myelin information may improve the understanding of the disease pathogenesis and lesion characterization, which are limited by the co-variation of iron and myelin in lesions and surrounding areas<sup>39,40</sup>. Another application is AD where amyloid plaque, which is diamagnetic<sup>41</sup>, is one of the histopathological hallmarks of the disease. The magnetic property of the plaque is changed to be paramagnetic when iron accumulates in the plaque<sup>42</sup>. The resulting paramagnetic property of the amyloid plaque has been captured in  $R_2^*$  and QSM<sup>43,44</sup>. The  $\chi$ -separation method may distinguish paramagnetic iron from diamagnetic amyloid plaque, potentially introducing a new AD imaging biomarker.

In this work, the positive and negative susceptibility maps are regarded as markers for iron and myelin, respectively, assuming the two are the only sources of magnetic susceptibility in the brain. The assumption is supported by previous studies<sup>12,45</sup>. Although rare, however, additional susceptibility sources such as calcium<sup>46</sup> and copper<sup>47</sup> may exist particularly in pathological conditions. Therefore, interpreting the results requires caution.

White matter has a complex microstructural geometry, which is not captured in our model, potentially creating errors in the susceptibility estimation. Despite this microstructural environment of the brain, our *ex-vivo* and *in-vivo* results show the potential of  $\chi$ -separation in identifying the distribution of paramagnetic (i.e., iron) and diamagnetic (i.e., myelin) sources (Figs. 4 and 6). Recently, efforts have been made to build a susceptibility model of white matter, suggesting the susceptibility source (i.e., myelin) in the hollow cylinders<sup>48,49</sup> with anisotropic effects<sup>50,51</sup>. Our model may be extended to incorporate this model and improve the accuracy when additional information such as fiber orientation is included. In such a model, the negative relaxometric constant can be formulated as a function of the fiber orientation.

Our model is established under the hypothesis that  $R_2'$  and frequency shift are solely determined by susceptibility concentration in the static dephasing regime. However, additional contrast sources such as chemical exchange may contribute to frequency shift and/or  $R_2'$ , although the effect size is smaller than that of susceptibility<sup>52,53</sup>. Additionally, the static dephasing condition may or may not hold for biological tissues and is affected by water diffusivity, and the size, geometry, and characteristic frequency of susceptibility sources<sup>12,54</sup>, influencing the relaxometric constant<sup>55</sup>. If the static dephasing condition breaks,  $R_2$  and  $R_2^*$  measurements can be changed by sequence parameters such as the echo space in spin echo<sup>56,57</sup>, affecting  $\chi$ -separation results.

The relaxometric constants in the simulation and phantom experiment were estimated by changing the source concentrations and measuring the corresponding  $R_2'$  changes. On the other hand, the *in-vivo* constant was estimated from deep gray matter ROIs and was used for both positive and negative relaxometric constants due to the absence of knowledge on the source concentrations. Although assumed to be constant in our experiment, the *in-vivo* relaxometric constant may vary across brain regions, influenced by the size, geometry, and characteristic frequency of susceptibility sources<sup>58–60</sup>. A further technique needs to be developed for an accurate measurement of the value. When we performed the  $\chi$ -separation reconstruction of the computer simulation and *in-vivo* data for a range of the relaxometric constant (75% to 125% of the original value), the susceptibility estimations showed qualitatively similar contrasts (Supplementary Figure. 9), suggesting that our *in-vivo* results are at least qualitatively relevant.

In the Monte-Carlo simulation, the susceptibility measurements from  $\chi$ -separation revealed slight underestimation when compared to the assigned susceptibility values (slopes of the linear lines: 0.99 in Fig. 2h). This underestimation can be explained by the numerical errors from a finite sampling of the dipole pattern as demonstrated in a previous study<sup>61</sup>.

In the phantom experiment, the susceptibility sources, especially  $\text{CaCO}_3$ , were not fully resolved in water, resulting in the aggregation of the sources. This aggregation is observed as a few spotty variations in the cylinders (Fig. 3) and maybe a source for the estimation errors in the  $\chi$ -separation results (Fig. 3f; Supplementary Figure 3d and e; Supplementary Figure 4).

In Figs. 5 and 7, negative susceptibility values are observed in voxels near large

vessels despite paramagnetic deoxyhemoglobin in the vessels. This error is due to the macroscopic field inhomogeneity effects from the vessels, creating non-local  $R_2'$ . This condition violates our assumption of fully localized  $R_2'$  in Eq. 4, creating artifacts in the results. In addition to this artifact, additional artifacts from large  $B_0$  field inhomogeneity, inaccurate background field removal, and fiber orientation effects, that are observed in conventional QSM, are also noticeable in  $\chi$ -separation (Supplementary Figure 10). Further technical development is expected to remove these artifacts and to improve the image quality of  $\chi$ -separation.

## OUTLOOK

We have demonstrated that a new biophysical model, describing the individual contribution of the positive and negative susceptibility sources to MRI signals, enables us to generate the maps of positive (i.e., iron) and negative (i.e., myelin) susceptibility sources in the human brain. This new technology was validated using computer simulation and experimental phantom and applied to *ex-vivo* and *in-vivo* human brains, producing high quality images of iron and myelin non-invasively. The results of healthy volunteers illustrate exquisite details of histologically well-known information of iron and myelin distributions, localizing structures such as nucleus dorsomedialis and pulvinar in thalamus. The images from multiple sclerosis patients reveal distinct characteristics of a few multiple sclerosis lesions such as iron-rim lesion and demyelinated lesion with iron depletion. The acquisition of  $\chi$ -separation data takes less than 20 min of MRI scan time, which can be further reduced with currently available fast imaging approaches, and, therefore, can be used as a practical tool for imaging microstructural information of the brain. Clinically, the technique could lead to *in-vivo* monitoring of pathogenesis of neurological diseases that entail changes in iron and myelin. It could also be applicable to neuroscience studies, exploring personalized localization of deep gray matter nuclei or identifying activity-induced myelin changes from neuroplasticity.



## METHODS

### *Monte-Carlo simulation*

To validate the two susceptibility models (Eqs. 2 and 4), and the  $\chi$ -separation method (Eq. 5), a Monte-Carlo simulation was performed. A total of nine segments were designed to have the nine different combinations of susceptibility source compositions (positive-source-only, negative-source-only, and sum of the positive and negative sources) and susceptibility concentrations ( $\pm 0.0125$ ,  $\pm 0.025$ , and  $\pm 0.0375$  ppm) (Fig. 2a-b). Each segment had  $26 \times 26 \times 32$  voxels, in which existed a cylinder (diameter: 8 voxels; length: 32 voxels) containing susceptibility sources (radius: 1  $\mu\text{m}$ ; susceptibility:  $+520^{20}$  or  $-520$  ppm). The field perturbation from the susceptibility sources was calculated using Maxwell's equation<sup>62</sup>, assuming the  $B_0$  field of 3 T. The longitudinal axis of the cylinders was assigned to be perpendicular to the  $B_0$  field. In each voxel, 1000 protons performed random walks, following Gaussian diffusion with the diffusion coefficient of 1  $\mu\text{m}^2/\text{ms}$ . Each proton had a unit magnetization and  $R_2$  of 10 Hz. In each time step (100  $\mu\text{s}$ ), the phase of the proton magnetization was accumulated by the susceptibility-induced field. Then, the voxel-averaged signal was calculated for the echo time (TE) of 2.6 ms to 27.1 ms with the echo spacing of 4.9 ms. This simulation was repeated 444 times with randomly repositioned protons and susceptibility sources, and the results were averaged for each voxel. After that, the magnitude signal decay was fitted to an exponential model to estimate  $R_2^*$ , whereas the phase evolution was fitted to a linear model to measure frequency shift. The  $R_2'$  map was calculated by subtracting the  $R_2$  from the  $R_2^*$  map. Other details of the simulation are described in Supplementary Information. The simulation was performed using 12 GPUs (Nvidia GTX 1080Ti, Santa Clara, CA), and the total simulation time was 21 days.

The relaxometric constants were determined by the slope of the linear regression line of the averaged  $R_2'$  values with respect to the absolute values of the assigned susceptibility in the positive-source-only cylinders for  $\overline{D_{r,pos}}$  and the negative-source-only cylinders for  $\overline{D_{r,neg}}$ . After that, the  $\chi$ -separation algorithm was applied to each segment, reconstructing the positive and negative susceptibility maps. The mean susceptibility value of each cylinder was compared with the assigned value. For analysis, linear regression was performed for the susceptibility values from the positive-source-only and negative-source-only cylinders and for those from the mixed-source cylinders.



491

## 492 *Phantom experiment*

493 For the phantom experiment, a large cylindrical container (diameter: 120 mm, length:  
494 92 mm) was filled with 1.5% agarose gel (Agarose ME, Daejung, Siheung, Republic of  
495 Korea). Before the gel hardened, a plastic cast was position to form a  $3 \times 3$  hollow cylinder  
496 array (cylinder diameter: 12 mm, length: 46 mm). These hollow cylinders were filled with  
497 different compositions and concentrations of susceptibility sources mixed with 1.5% agarose  
498 gel. For the susceptibility sources, iron oxide ( $\text{Fe}_3\text{O}_4$ , Bangs Laboratories Inc., Fisher, IN,  
499 USA) was used for positive susceptibility, and calcium carbonate powder ( $\text{CaCO}_3$ , Yakuri  
500 Pure Chemicals, Kyoto, Japan) for negative susceptibility. In the first-row cylinders of the  
501 array, the iron oxide-containing gel of 0.25, 0.50, and 0.75 mg/ml iron oxide concentrations  
502 was assigned. In the second row, the calcium carbonate powder-containing gel of 12.5, 25.0,  
503 and 37.5 mg/ml calcium carbonate concentrations was assigned. In the third-row cylinders,  
504 the mixtures of the iron oxide and calcium carbonate were created with the concentrations as  
505 the sum of the first two rows (Fig. 3c). To prevent precipitation of the susceptibility sources,  
506 an agarose solution was shaken before pouring into the hollow cylinder.

507 The phantom was scanned at 3 T MRI (Siemens Tim Trio, Erlangen, Germany). The  
508 longitudinal axis of the small cylinders was placed perpendicular to the  $B_0$  field. For  $R_2^*$  and  
509 frequency shift, 3D multi-echo gradient-echo were acquired with the following parameters:  
510 field of view (FOV) =  $192 \times 192 \times 120 \text{ mm}^3$ , voxel size =  $1 \times 1 \times 2 \text{ mm}^3$ , repetition time (TR)  
511 = 60 ms, echo time (TE) = 2.6 to 27.1 ms with the echo spacing of 4.9 ms, bandwidth = 300  
512 Hz/pixel, flip angle =  $30^\circ$ , and total acquisition time = 11.6 min. For  $R_2$ , 2D multi-echo spin-  
513 echo data were acquired: FOV =  $192 \times 192 \text{ mm}^2$ , voxel size =  $1 \times 1 \text{ mm}^2$ , slice thickness = 2  
514 mm, number of slices = 40, TR = 4000 ms, concatenation factor = 2, TE = 9 to 90 ms with  
515 the echo spacing of 9 ms, bandwidth = 300 Hz/pixel, and total acquisition time = 29.6 min.

516 After the acquisition, k-space data of all channels were reconstructed and then  
517 combined using the sum-of-squares for magnitude and MCPC-3D for phase<sup>63</sup>. To estimate the  
518 frequency shift, the multi-echo phase data were fitted to a linear model. Then, the result was  
519 spatially unwrapped<sup>64</sup> and background-field-removed<sup>65</sup>, producing a frequency shift map.  
520 From the frequency map, a conventional QSM map was reconstructed using the MEDI  
521 Toolbox (<http://pre.weill.cornell.edu/mri/pages/qsm.html><sup>66</sup>). For  $R_2^*$  mapping, the

magnitudes of multi-echo gradient echo signals were fitted to a mono-exponential decay function. For  $R_2$  mapping, the multi-echo spin-echo magnitude images were matched with a computer-simulated dictionary of spin-echo decay embedded with the stimulated echo correction<sup>67</sup>. Then, an  $R_2'$  map was calculated by a voxel-wise subtraction of  $R_2$  from  $R_2^*$ . Negative  $R_2'$  values were refined to zero to enforce physics. The same reconstruction approach was performed for subsequent sections unless stated. The relaxometric constants were determined as the slope of the linear regression line of the mean  $R_2'$  with respect to the susceptibility values (estimated by the conventional QSM) in the positive-source-only cylinders for  $\overline{D_{r,pos}}$  and the negative-source-only cylinders for  $\overline{D_{r,neg}}$ . The voxels with extreme  $R_2'$  ( $> 25$  Hz or  $< 2$  Hz), which is most likely from the aggregation of the susceptibility sources, were excluded in the calculation. Finally, the positive and negative susceptibility maps were generated by  $\chi$ -separation. To demonstrate successful susceptibility separation, the positive and negative susceptibility values in the mixed-source cylinders were compared to those in the single-source-only cylinders using a linear regression analysis.

### ***Ex-vivo experiment***

To demonstrate the specificity of  $\chi$ -separation to iron and myelin in a biological tissue, an *ex-vivo* human brain specimen, containing V1, was scanned. The results were compared with iron and myelin distributions measured by LA-ICP-MS and LFB myelin stain, respectively. The specimen was fixed in the 4% paraformaldehyde solution for four weeks after an autopsy, and then incubated in 0.1 M phosphate-buffered saline for seven days before being scanned at 7 T MRI (Siemens Terra, Erlangen, Germany). For the scan, 3D multi-echo gradient-echo data were acquired with the following parameters: FOV =  $77 \times 77 \times 64$  mm<sup>3</sup>, voxel size =  $0.3 \times 0.3 \times 0.5$  mm<sup>3</sup>, TR = 300 ms, TE = 3.9 to 39.8 ms with the echo spacing of 6.5 ms, flip angle = 45°, bandwidth = 300 Hz/pixel, two averages, and total acquisition time = 4.8 h. For 3D multi-echo spin-echo, the parameters had the same FOV and resolution as the gradient-echo acquisition, TR = 450 ms, TE = 14 to 70 ms with the echo spacing of 14 ms, bandwidth = 272 Hz/pixel, three averages, and total acquisition time = 10.6 h. The data were reconstructed in the same procedures as described in the phantom experiment. For  $\chi$ -separation, the relaxometric constants from the health volunteers (see the next section) were used after scaling for the field strength difference (7 T vs. 3 T).

After the MRI scan, the specimen was paraffin-embedded and cut into 20- $\mu$ m thick sections. The sections were utilized for the LFB myelin staining and LA-ICP-MS. For the myelin staining, the sections were deparaffinized and then immersed in a 0.1% LFB solution (LFB MBS 1.0 g (S3382, Sigma-Aldrich, St. Louis Luis, Mo, USA), 95% ethyl alcohol 1000 mL, and glacial acetic acid 5.0 mL (A6283, Sigma-Aldrich, St. Louis Luis, Mo, USA)) at 56  $^{\circ}$ C for 24 hours. The stain section was immersed in a 0.05% lithium carbonate solution (62470, Sigma-Aldrich, St. Louis Luis, Mo, USA) for tens of seconds for the differentiation<sup>28</sup> and then imaged in a scanner with  $\times 10$  magnification (Axio Scan.Z1 slide scanner, Zeiss, Oberkochen, Germany). For the LA-ICP-MS, one of the sections was ablated using a 1030 nm femto-second pulsed laser system (J200 Femto iX, Applied Spectra Inc, West Sacramento, CA, USA) with the following parameters: laser spot diameter = 80  $\mu$ m, line scan speed = 200  $\mu$ m/s, repetition rate = 50 Hz, and raster spacing = 120  $\mu$ m. The ablated tissue was transported by helium gas (0.9 L/min) with make-up argon gas (0.7 L/min) to a quadrupole ICP-MS device (iCAP TQ, ThermoFisher Scientific, Bremen, Germany), measuring <sup>56</sup>Fe and <sup>13</sup>C. The iron distribution ( $Fe_{LA-ICP-MS}$ ) was calculated as the signal intensity ratio of <sup>56</sup>Fe to <sup>13</sup>C to compensate for a system drift, assuming <sup>13</sup>C as a reference (see Supplementary Figure 11)<sup>68</sup>. The chronological mass spectrum measurements were reshaped into a 2D image with the spatial resolution of 120  $\mu$ m  $\times$  40  $\mu$ m.

### ***In-vivo experiment: healthy volunteers***

Six healthy volunteers (age =  $33.7 \pm 14.6$  years; 5 females and 1 male) were scanned at 3 T MRI (Siemens Tim Trio, Erlangen, Germany). All volunteers signed a written consent form approved by the institutional review board (IRB). The acquisition parameters for 3D multi-echo gradient-echo were FOV = 192  $\times$  192  $\times$  96 mm<sup>3</sup>, voxel size = 1  $\times$  1  $\times$  2 mm<sup>3</sup>, TR = 64 ms, TE = 2.9 to 25.9 ms with the echo spacing of 4.6 ms, bandwidth = 300 Hz/pixel, flip angle = 22 $^{\circ}$ , parallel imaging factor = 2, and total acquisition time = 7.0 min. For 2D multi-echo spin-echo, the parameters were FOV = 192  $\times$  192 mm<sup>2</sup>, voxel size = 1  $\times$  1 mm<sup>2</sup>, slice thickness = 2 mm, number of slices = 40, TR = 3860 ms, TE = 15 to 90 ms with the echo spacing of 15 ms, bandwidth = 100 Hz/pixel, and total acquisition time = 12.4 min. The data were reconstructed as described in the phantom experiment. The relaxometric constant was estimated from five deep gray matter ROIs that have primarily positive susceptibility: globus

pallidus, putamen, caudate nucleus, substantia nigra, and red nucleus. The constant ( $\overline{D_{r,pos}}$ ) was determined by the slope of the linear regression line of the ROI-averaged  $R_2'$  values with respect to the susceptibility values (by the conventional QSM). For  $\overline{D_{r,neg}}$ , the same value as  $\overline{D_{r,pos}}$  was used (see Discussion). After the reconstruction, the positive and negative susceptibility maps were compared with the histologically stained iron and myelin images from literatures<sup>30–32</sup>.

### ***In-vivo experiment: multiple sclerosis patients***

Two MS patients (Patient 1: 34-year-old male; Patient 2: 23-year-old female; IRB-approved) were scanned using 3 T MRI (Philips Ingenia, Amsterdam, Netherlands). 3D multi-echo gradient-echo data were acquired with the following parameters: FOV =  $216 \times 216 \times 144 \text{ mm}^3$ , voxel size =  $0.5 \times 0.5 \times 2 \text{ mm}^3$ , TR = 42 ms, TE = 5.8 to 36.7 ms with the echo spacing of 6.2 ms, bandwidth = 255 Hz/pixel, flip angle =  $17^\circ$ , parallel imaging factor =  $2.5 \times 1.4$ , and total acquisition time = 5.1 min. For Patient 1, 2D multi-echo spin-echo data were acquired with the following parameters: FOV =  $216 \times 216 \text{ mm}^2$ , voxel size =  $0.5 \times 0.5 \text{ mm}^2$ , slice thickness = 2 mm, number of slices = 14, TR = 1800 ms, and TE = 10 to 90 ms with the echo spacing of 10 ms, bandwidth = 301 Hz/pixel, parallel imaging factor = 1.3, and total acquisition time = 7.8 min. For Patient 2, the same 2D multi-echo spin-echo data were acquired except for the following parameters: number of slices = 24, TR = 3300 ms, and TE = 20 to 100 ms with the echo spacing of 20 ms, bandwidth = 218 Hz/pixel, parallel imaging factor = 2.5, and total acquisition time = 7.2 min. For the clinical assessment of MS lesions, T<sub>1</sub>-weighted, T<sub>2</sub>-weighted, FLAIR, and gadolinium contrast-enhanced (CE) T<sub>1</sub>-weighted images were obtained (see Supplementary Information). The reconstruction was conducted in the same procedure as in the healthy volunteers except for the magnitude and phase generation which was performed by the scanner.

All data processing was performed using MATLAB (MATLAB 2020a, MathWorks Inc., Natick, MA, USA).

613     **ACKNOWLEDGMENTS**

614             This research was supported by the National Research Foundation of Korea grant  
615     funded by the Korea government (NRF-2018R1A2B3008445) and the Grant-in-Aid for  
616     Scientific Research (KAKENHI-19K22985) from Japan Society for the Promotion of Science.  
617     We thank Professor Norihiro Sadato for his support of this project and the Institute for Basic  
618     Science (IBS) Center for Neuroscience Imaging Research (IBS-R015-D1) for providing MRI  
619     time and professional technical support.

620

621

622

623

## REFERENCES

1. Ramón y Cajal, S. La retine des vertebres. (Cellule, 1893).
2. Brodmann, K. Vergleichende Lokalisationslehre der Grosshirnrinde in ihren Prinzipien dargestellt auf Grund des Zellenbaues. (Barth, 1909).
3. Singh, S. K. et al. Identification of human brain tumour initiating cells. *Nature* 432, 396–401 (2004).
4. Ding, S. et al. Comprehensive cellular-resolution atlas of the adult human brain. *J Comp Neurol* 524, 3127–3481 (2016).
5. Weiskopf, N., Mohammadi, S., Lutti, A. & Callaghan, M. F. Advances in MRI-based computational neuroanatomy: from morphometry to in-vivo histology. *Curr Opin Neurol* 28, 313–322 (2015).
6. Zhang, H., Schneider, T., Wheeler-Kingshott, C. A. & Alexander, D. C. NODDI: Practical in vivo neurite orientation dispersion and density imaging of the human brain. *Neuroimage* 61, 1000–1016 (2012).
7. MacKay, A. L. & Laule, C. Magnetic Resonance of Myelin Water: An in vivo Marker for Myelin. *Adv Neurol* 2, 71–91 (2016).
8. Haacke, E. M. et al. Imaging iron stores in the brain using magnetic resonance imaging. *Magn Reson Imaging* 23, 1–25 (2005).
9. Duyn, J. H. et al. High-field MRI of brain cortical substructure based on signal phase. *Proc National Acad Sci* 104, 11796–11801 (2007).
10. Sung, Y. H. et al. Differential involvement of nigral subregions in idiopathic parkinson's disease. *Hum Brain Mapp* 39, 542–553 (2018).
11. Kirilina, E. et al. Superficial white matter imaging: Contrast mechanisms and whole-brain in vivo mapping. *Sci Adv* 6, eaaz9281 (2020).
12. Duyn, J. H. & Schenck, J. Contributions to magnetic susceptibility of brain tissue. *Nmr Biomed* 30, e3546 (2017).
13. Ward, R. J., Zucca, F. A., Duyn, J. H., Crichton, R. R. & Zecca, L. The role of iron in brain ageing and neurodegenerative disorders. *Lancet Neurology* 13, 1045–1060 (2014).
14. Stephenson, E., Nathoo, N., Mahjoub, Y., Dunn, J. F. & Yong, V. W. Iron in multiple sclerosis: roles in neurodegeneration and repair. *Nat Rev Neurol* 10, 459–468 (2014).
15. Zecca, L., Youdim, M. B. H., Riederer, P., Connor, J. R. & Crichton, R. R. Iron, brain ageing and neurodegenerative disorders. *Nat Rev Neurosci* 5, 863–873 (2004).
16. Sowell, E. R. et al. Mapping cortical change across the human life span. *Nat Neurosci* 6, 309–315 (2003).
17. McKenzie, I. A. et al. Motor skill learning requires active central myelination. *Science* 346, 318–322 (2014).
18. Nave, K.-A. Myelination and support of axonal integrity by glia. *Nature* 468, 244–252 (2010).
19. Compston, A. & Coles, A. Multiple sclerosis. *Lancet* 372, 1502–1517 (2008).

658 20. Schenck, J. F. The role of magnetic susceptibility in magnetic resonance imaging: MRI magnetic  
659 compatibility of the first and second kinds. *Med Phys* 23, 815–850 (1996).

660 21. Yablonskiy, D. A. & Haacke, E. M. Theory of NMR signal behavior in magnetically inhomogeneous tissues:  
661 The static dephasing regime. *Magnet Reson Med* 32, 749–763 (1994).

662 22. Schweser, F., Deistung, A., Lehr, B. W. & Reichenbach, J. R. Quantitative imaging of intrinsic magnetic  
663 tissue properties using MRI signal phase: an approach to in vivo brain iron metabolism? *Neuroimage* 54, 2789  
664 2807 (2011).

665 23. Stüber, C., Pitt, D. & Wang, Y. Iron in Multiple Sclerosis and Its Noninvasive Imaging with Quantitative  
666 Susceptibility Mapping. *Int J Mol Sci* 17, 100 (2016).

667 24. Salomir, R., Senneville, B. D. de & Moonen, C. T. A fast calculation method for magnetic field  
668 inhomogeneity due to an arbitrary distribution of bulk susceptibility. *Concepts Magnetic Reson Part B Magnetic*  
669 *Reson Eng* 19B, 26–34 (2003).

670 25. Marques, J. P. & Bowtell, R. Application of a Fourier-based method for rapid calculation of field  
671 inhomogeneity due to spatial variation of magnetic susceptibility. *Concepts Magnetic Reson Part B Magnetic*  
672 *Reson Eng* 25B, 65–78 (2005).

673 26. Rochefort, L. de, Brown, R., Prince, M. R. & Wang, Y. Quantitative MR susceptibility mapping using piece-  
674 wise constant regularized inversion of the magnetic field. *Magnet Reson Med* 60, 1003–1009 (2008).

675 27. Shmueli, K. et al. Magnetic susceptibility mapping of brain tissue in vivo using MRI phase data. *Magnet*  
676 *Reson Med* 62, 1510–1522 (2009).

677 28. Fukunaga, M. et al. Layer-specific variation of iron content in cerebral cortex as a source of MRI contrast.  
678 *Proc National Acad Sci* 107, 3834–3839 (2010).

679 29. Sachs, H. Das Hemisphärenmark des menschlichen Grosshirns. *Dmw - Deutsche Medizinische*  
680 *Wochenschrift* 19, 651–652 (1893).

681 30. Drayer, B. et al. MRI of brain iron. *Am J Roentgenol* 147, 103–110 (1986).

682 31. Schaltenbrand, G. & Wahren, W. Atlas for stereotaxy of the human brain. (Thieme, 1977).

683 32. Naidich, T. P., Castillo, M., Cha, S. & Smirniotopoulos, J. G. Imaging of the brain. (Saunders, 2013).

684 33. Bagnato, F. et al. Tracking iron in multiple sclerosis: a combined imaging and histopathological study at 7  
685 Tesla. *Brain J Neurology* 134, 3602–15 (2011).

686 34. Hametner, S. et al. Iron and neurodegeneration in the multiple sclerosis brain. *Ann Neurol* 74, 848–61  
687 (2013).

688 35. Papavassiliou, E. et al. Thalamic Deep Brain Stimulation for Essential Tremor: Relation of Lead Location to  
689 Outcome. *Neurosurgery* 54, A24 (2004).

690 36. Lipsman, N. et al. MR-guided focused ultrasound thalamotomy for essential tremor: a proof-of-concept  
691 study. *Lancet Neurology* 12, 462–468 (2013).

692 37. Glasser, M. F. et al. A multi-modal parcellation of human cerebral cortex. *Nature* 536, 171–178 (2016).

693 38. Alemán-Gómez, Y. et al. Partial-volume modeling reveals reduced gray matter in specific thalamic nuclei  
694 early in the time course of psychosis and chronic schizophrenia. *Hum Brain Mapp* 41, 4041–4061 (2020).



695 39. Wisniewski, C. et al. Quantitative susceptibility mapping (QSM) of white matter multiple sclerosis lesions:  
696 Interpreting positive susceptibility and the presence of iron: Iron and Myelin Content of MS Lesions with MRI.  
697 *Magnet Reson Med* 74, 564–570 (2015).

698 40. Wiggermann, V. et al. Susceptibility-sensitive MRI of multiple sclerosis lesions and the impact of normal-  
699 appearing white matter changes. *Nmr Biomed* 30, e3727 (2017).

700 41. Gong, N.-J., Dibb, R., Bulk, M., Weerd, L. van der & Liu, C. Imaging beta amyloid aggregation and iron  
701 accumulation in Alzheimer's disease using quantitative susceptibility mapping MRI. *Neuroimage* 191, 176–185  
702 (2019).

703 42. Telling, N. D. et al. Iron Biochemistry is Correlated with Amyloid Plaque Morphology in an Established  
704 Mouse Model of Alzheimer's Disease. *Cell Chem Biol* 24, 1205–1215.e3 (2017).

705 43. Jack, C. R. et al. In vivo visualization of Alzheimer's amyloid plaques by magnetic resonance imaging in  
706 transgenic mice without a contrast agent. *Magnet Reson Med* 52, 1263–1271 (2004).

707 44. Tuzzi, E. et al. Ultra-High Field MRI in Alzheimer's Disease: Effective Transverse Relaxation Rate and  
708 Quantitative Susceptibility Mapping of Human Brain In Vivo and Ex Vivo compared to Histology. *J*  
709 *Alzheimer's Dis* 73, 1481–1499 (2020).

710 45. Hametner, S. et al. The influence of brain iron and myelin on magnetic susceptibility and effective transverse  
711 relaxation - A biochemical and histological validation study. *Neuroimage* 179, 117–133 (2018).

712 46. Chen, W. et al. Intracranial Calcifications and Hemorrhages: Characterization with Quantitative  
713 Susceptibility Mapping. *Radiology* 270, 496–505 (2014).

714 47. Fritzsche, D. et al. Seven-Tesla Magnetic Resonance Imaging in Wilson Disease Using Quantitative  
715 Susceptibility Mapping for Measurement of Copper Accumulation. *Invest Radiol* 49, 299–306 (2014).

716 48. Wharton, S. & Bowtell, R. Fiber orientation-dependent white matter contrast in gradient echo MRI. *Proc*  
717 *National Acad Sci* 109, 18559–18564 (2012).

718 49. Sati, P. et al. Micro-compartment specific T2\* relaxation in the brain. *Neuroimage* 77, 268–278 (2013).

719 50. Lee, J. et al. Sensitivity of MRI resonance frequency to the orientation of brain tissue microstructure. *P Natl*  
720 *Acad Sci Usa* 107, 5130–5 (2010).

721 51. Wharton, S. & Bowtell, R. Effects of white matter microstructure on phase and susceptibility maps. *Magnet*  
722 *Reson Med* 73, 1258–1269 (2015).

723 52. Shmueli, K., Dodd, S. J., Li, T.-Q. & Duyn, J. H. The contribution of chemical exchange to MRI frequency  
724 shifts in brain tissue. *Magnet Reson Med* 65, 35–43 (2011).

725 53. Eun, H., Jeong, H., Lee, J., Shin, H. & Lee, J. A geometric approach to separate the effects of magnetic  
726 susceptibility and chemical shift/exchange in a phantom with isotropic magnetic susceptibility. *Magnet Reson*  
727 *Med* (2020) doi:10.1002/mrm.28408.

728 54. Brammerloh, M. et al. Toward an early diagnostic marker of Parkinson's: measuring iron in dopaminergic  
729 neurons with MR relaxometry. *Biorxiv* 2020.07.01.170563 (2020) doi:10.1101/2020.07.01.170563.

730 55. Yung, K.-T. Empirical models of transverse relaxation for spherical magnetic perturbations. *Magn Reson*  
731 *Imaging* 21, 451–463 (2003).

732 56. Muller, R. N., Gillis, P., Moyné, F. & Roch, A. Transverse relaxivity of particulate MRI contrast media: From



theories to experiments. *Magnet Reson Med* 22, 178–182 (1991).

57. Ye, F. Q. & Allen, P. S. Relaxation enhancement of the transverse magnetization of water protons in paramagnetic suspensions of red blood cells. *Magnet Reson Med* 34, 713–720 (1995).

58. Taege, Y. et al. Assessment of mesoscopic properties of deep gray matter iron through a model-based simultaneous analysis of magnetic susceptibility and  $R2^*$  - A pilot study in patients with multiple sclerosis and normal controls. *Neuroimage* 186, 308–320 (2019).

59. Schenck, J. F. & Zimmerman, E. A. High-field magnetic resonance imaging of brain iron: birth of a biomarker? *Nmr Biomed* 17, 433–445 (2004).

60. Gossuin, Y., Muller, R. N. & Gillis, P. Relaxation induced by ferritin: a better understanding for an improved MRI iron quantification. *Nmr Biomed* 17, 427–432 (2004).

61. Zhou, D., Cho, J., Zhang, J., Spincemaille, P. & Wang, Y. Susceptibility underestimation in a high-field susceptibility phantom: Dependence on imaging resolution, magnitude contrast, and other parameters. *Magnet Reson Med* 78, 1080–1086 (2017).

62. Li, L. & Leigh, J. S. Quantifying arbitrary magnetic susceptibility distributions with MR. *Magnet Reson Med* 51, 1077–1082 (2004).

63. Robinson, S., Grabner, G., Witoszynski, S. & Trattnig, S. Combining phase images from multi-channel RF coils using 3D phase offset maps derived from a dual-echo scan. *Magnet Reson Med* 65, 1638–1648 (2011).

64. Cusack, R. & Papadakis, N. New Robust 3-D Phase Unwrapping Algorithms: Application to Magnetic Field Mapping and Undistorting Echoplanar Images. *Neuroimage* 16, 754–764 (2002).

65. Wu, B., Li, W., Guidon, A. & Liu, C. Whole brain susceptibility mapping using compressed sensing. *Magnet Reson Med* 67, 137–147 (2012).

66. Liu, Z., Spincemaille, P., Yao, Y., Zhang, Y. & Wang, Y. MEDI+0: Morphology enabled dipole inversion with automatic uniform cerebrospinal fluid zero reference for quantitative susceptibility mapping. *Magnet Reson Med* 79, 2795–2803 (2018).

67. McPhee, K. C. & Wilman, A. H. T2 quantification from only proton density and T2-weighted MRI by modelling actual refocusing angles. *Neuroimage* 118, 642–650 (2015).

68. Lee, H. et al. MRI T2 and T2\* relaxometry to visualize neuromelanin in the dorsal substantia nigra pars compacta. *Neuroimage* 211, 116625 (2020).